J Nanopart Res (2022) 24: 126
https://doi.org/10.1007/s11051-022-05509-0

RESEARCH PAPER

Preparation and electrochemical performance of nanostructured Co_3O_4 particles

Phimmani Tharasan · Monthira Somprasong · Nititorn Kenyota · Nattakan Kanjana · Wasan Maiaugree · Wirat Jareonboon · Paveena Laokul

Received: 30 December 2021 / Accepted: 2 June 2022 / Published online: 16 June 2022

Abstract The nanostructured Co_3O_4 particles were prepared by a simple and inexpensive precipitation method, which can be used as electrode materials in pseudocapacitive energy storage devices. The effect of temperature on the crystal structure and morphology of the material was discussed to obtain a suitable condition for the fabrication of the electrodes. The results showed that the Co_3O_4 calcined at 400 °C (C4) with an average particle size of 34.1 ± 4.0 nm is suitable for electrode fabrication. This is due to the superior electrical conductivity and high purity of the phase structure with a larger specific surface area and porosity compared to the samples calcined at 600 and 800 °C. Moreover, the different oxidation states of Co ions in electrochemical reactions are the main factor for the high capacitance values of the sample. The maximum specific capacitance of 115.3 F/g at a current density of 1 A/g was achieved by the C4 sample. The charge/discharge stability measurements with maximum a of 5000 cycles showed that the sample can achieve excellent retention of specific capacitance of almost 100% for up to 1900 cycles at a current density of 5 A/g.

Keywords Co_3O_4 nanoparticles · Precipitation method · Electrochemical properties · Supercapacitors · Life cycle stability · Energy storage

Introduction

In recent decades, preparation methods of nanostructural materials with various morphologies, such as nanoparticles [1], nanotubes [2], nanowires [3], and nanosheets [4], among others, have facilitated the expression of distinctive physical and chemical properties appropriate to specific applications [5]. Recently, transition metal oxide nanoparticles have received considerable interest owing to their wide range of applications, such as in photocatalysis [6], gas sensors [7], magnetic materials [8], and electrode materials for supercapacitors [9], among others. This is due to their superior physical, chemical, and electrical properties. Among transition metal group compounds, such as RuO_2, MnO_2, NiO, and Fe_3O_4, cobalt

Supplementary Information The online version contains supplementary material available at https://doi.org/10.1007/s11051-022-05509-0.

P. Tharasan · M. Somprasong · N. Kenyota · N. Kanjana · P. Laokul (✉)
Department of Physics, Faculty of Science, Mahasarakham University, Khamriag Sub-District, Khantarawichai District, Mahasarakham 44150, Thailand
e-mail: paveena@msu.ac.th

W. Maiaugree
Division of Physics, Faculty of Science and Technology, Thammasat University, Bangkok 12120, Pathum Thani, Thailand

W. Jareonboon
Department of Physics, Faculty of Science, Khon Kaen University, Khon Kaen 40002, Thailand

oxide (Co_3O_4) is a spinel structured p-type semiconducting material with chemical stability at high temperatures. Although Co has no advantage over Fe and Ni, Co_3O_4 is one of the attractive transition metal oxides for supercapacitor application compared to materials with excellent capacitor properties such as RuO_2 due to its lower cost, good redox properties, controllable particle size and shape, high chemical and structural stability and high theoretical capacitance (~3650 F/g). [8–11]. Additionally, cobalt oxide is a polymorphic material that can be found in three different forms in nature, CoO, Co_2O_3, and Co_3O_4. The Co_3O_4 form has become an alternative material for supercapacitor electrode applications, replacing expensive and highly toxic metal oxides such as Ru_2O_3, the material with the highest specific pseudocapacitance currently known [5, 8]. Several methods have been reported to synthesize Co_3O_4 nanoparticles. They are categorized into either chemical or physical treatments, including hydrothermal, solvothermal, physical vapor deposition (PVD), chemical vapor deposition (CVD), solid-state reaction, sol–gel process, and precipitation methods [12]. Among the various approaches, precipitation is one of the most attractive methods to prepare these nanoparticles. This is because it can easily be used to control morphology and the size of the resulting particles. Additionally, it uses inexpensive synthetic precursors, low reaction temperatures, and produces highly homogenous products [10, 13].

The aim of this work is to develop a simple and inexpensive synthesis of uniform Co_3O_4 nanoparticles with high crystallinity by a precipitation method. The microstructure and surface properties of the as-synthesized powders were characterized using several techniques, including X-ray diffraction (XRD), field emission scanning electron microscopy (FESEM), transmission electron microscopy (TEM), and X-ray photoelectron spectroscopy (XPS), as well as the Brunauer–Emmett–Teller (BET) and Barrett–Joyner–Halenda (BJH) techniques. The calcined Co_3O_4 powders were used as raw materials to fabricate electrodes without either carbonization or alkali-activation process. The electrochemical properties of the cells were investigated using cyclic voltammetry (CV), galvanostatic charge/discharge (GCD), and electrochemical impedance spectroscopy (EIS). Analysis of the results showed that all samples produced had intrinsic pseudocapacity. A maximum specific capacitance of 115.27 F/g was achieved at a current density of 1 A/g within a potential window of 0.1 to 0.45 V. Interestingly, excellent long-term stability with 100% capacitance retention was achieved after 1900 charge/discharge cycles at a current density of 5 A/g.

Experimental methods

Material preparation

Cobalt tetraoxide nanoparticles (Co_3O_4 NPs) were synthesized via a precipitation method as previously described [10]. Typically, a 1:2 molar ratio of $Co(CH_3CO_2)_2{\cdot}4H_2O$ and NaOH solution were used as the starting materials. Initially, 1 M cobalt (II) acetate was dissolved in 20 ml distilled water with vigorous mixing on a hot plate stirrer at 80 °C for 30 min. After that, a 2 M NaOH solution was added dropwise into the above solution until the pH was 10. The reaction was then continued with magnetic stirring at 80 °C for 2 h. After producing a homogeneous mixture, the prepared solution was then left to stand overnight at room temperature. The precipitate was collected via centrifugation and washed several times with distilled water followed by ethanol and was subsequently dried in vacuum oven at 80 °C for 24 h. Finally, the obtained Co_3O_4 precursor powders were calcined for 3 h at different temperatures; 400, 600, and 800 °C, and referred to thereafter as the C4, C6, and C8 samples, respectively.

Characterizations

The structural properties of the samples were determined using XRD with Bruker D8 Advance equipment. Crystallite sizes were calculated from X-ray line broadening. Fourier transform infrared (FTIR) spectra were determined using a JASCO FT-IR-480 Plus spectrophotometer in the wavenumber range 4000–400 cm^{-1}. The microstructure and morphology of the materials were studied under FESEM (JEOL-JSM-7800F) and TEM (FEI Tecnai G2 20). XPS (AXIS Ultra DLD, Kratos Analytical) was employed to find the valance and chemical states of the calcined Co_3O_4 samples. The specific surface area was evaluated using the BET approach

through nitrogen adsorption–desorption isotherm measurements. Pore size distributions were analyzed by applying BJH methodology employing the desorption branch of the isotherms. Electrochemical properties were tested at room temperature in a beaker-type three-electrode system using 6 M KOH as an electrolyte solution. The calcined Co_3O_4 NPs were used as working electrodes. A platinum plate and saturated Ag/AgCl electrode were employed as counter and reference electrodes, respectively. The preparation of the electrodes and the experimental procedures are described as follows. First, a mixture of active materials, including Co_3O_4 powder, acetylene black, and polyvinylidene fluoride (PVDF), was dissolved in N-methyl-2-pyrrolidone (NMP) in a weight ratio of 80:10:10. The obtained paste was applied to a Ni foam substrate with an active area of 1×2 cm^2. This was then used as a current collector after being dried in a vacuum oven at 60 °C for 12 h. The specimens were uniaxially compressed under a load of 100 MPa and then impregnated with an electrolyte solution for 6 h prior to electrochemical testing. Cyclic voltammetry was carried out at room temperature at scan rates of 5, 10, 20, 50, and 100 mV/s under a potential window that ranged from − 0.1 to 0.45 V. Galvanostatic charge/discharge tests were performed employing current densities of 1, 2, 5, 10, and 20 A/g. The ESI spectra of the prepared working electrodes were measured using an AC-bias voltage of 5 mV in the frequency range of 0.01–100 kHz.

Results and discussion

Material characterizations

The crystal structures of the prepared Co_3O_4 NPs calcined at 400, 600, and 800 °C were determined using an XRD technique. The diffraction patterns of all the samples are shown in Fig. 1(a). It is notable that the diffraction peaks at around 31.3, 36.9, 38.6, 44.8, 55.7, 59.4, 65.2, 74.1, 77.3, 78.4, and 82.6° are analogous to (220), (311), (222), (400), (422), (511), (440), (620), (533), (622), and (444) lattice planes, respectively, of a cubic spinel, structured Co_3O_4 within a Fd3m space group. All diffraction peaks were consistent with the standard pattern, JCPDS No. 42–1467, with no trace of other phases or impurities. Additionally, the diffraction peaks became sharper and narrower as the calcination temperature increased from 400 to 800 °C. The average crystallite size of Co_3O_4 NPs was calculated using the diffraction peaks of the (220), (311), (400), (422), (511), and (440) planes employing the Debye–Scherer equation:

$$D = \frac{k\lambda}{\beta \cos\theta} \quad (1)$$

where D is the crystallite size, k is a constant with a value of 0.98, λ is the wavelength of the Cu–Kα radiation (1.5406 Å), β is the full width at half maximum (FWHM), and θ is the diffraction angle [14]. It can be clearly seen in Table 1 that the calculated crystallite size of the samples increased from 19.3 ± 1.4 nm

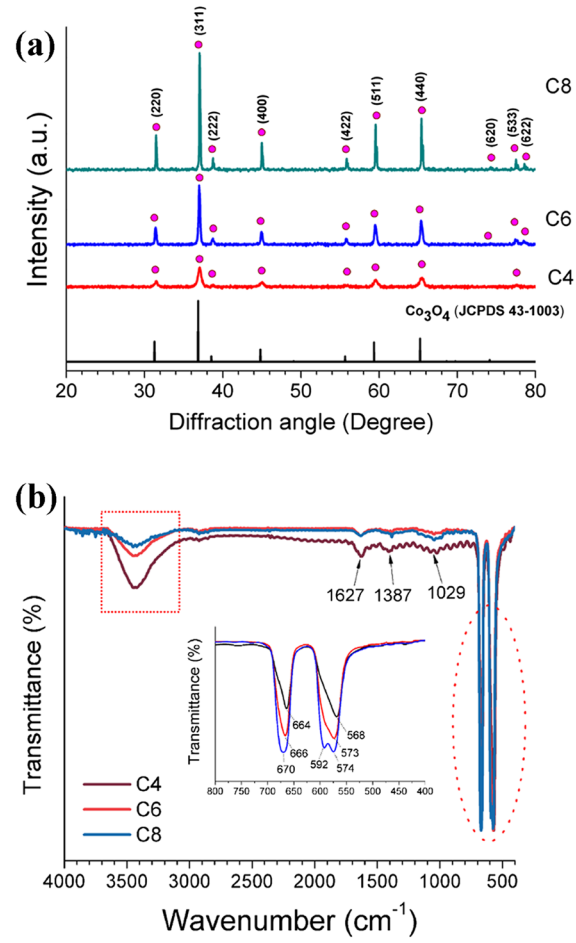

Fig. 1 **a** XRD patterns and **b** FTIR spectra of Co_3O_4 NPs calcined at different temperatures

to 98.0 ± 5.2 nm with increasing calcination temperature from 400 to 800 °C. Furthermore, the lattice parameters were calculated using the peak positions corresponding to the Co_3O_4 phase, and the results are shown in Table 1. The analysis of the results revealed that the lattice parameter tended to decrease from 8.089 to 8.083 Å with increasing calcination temperature from 400 to 800 °C. This is attributed to the increased thermal energy contributing to a more orderly arrangement of elemental ions, which is related to the size of the unit cells within the lattice structure of the materials [15].

FTIR spectra were recorded over the range of 4000–400 cm^{-1}, to determine the various functional groups associated with the calcined Co_3O_4 samples. In Fig. 1(b), the FTIR spectra display two distinct and sharp absorption bands at 572 and 667 cm^{-1}, which originate from the stretching vibration modes of the Co–O bonds. They confirm the formation of a spinel structure of Co_3O_4. From a refined analysis of the fingerprint area of the material, it was found that the peak at 572 cm^{-1} corresponded to the vibrations of the Co^{3+}–O bond in the octahedral sites. The peak at 667 cm^{-1} is attributed to the Co^{2+}–O bond in the tetrahedral sites of the spinel lattice structured Co_3O_4 [16, 17]. The minor peaks at 1029 and 1387 cm^{-1}, clearly observed in C4, were attributed to the C–O stretching vibration and the symmetric CH_3 deformations, respectively, due to the residual acetate group of the precursor [16]. The peaks at ~ 1627 cm^{-1} and the strong broadband in the range of 3000–3700 cm^{-1} were correlated with the bending and stretching modes of molecular water and hydrogen bonds, O–H groups adsorbed on the surface of Co_3O_4 nanoparticles [15–17]. Considering the absorption spectra of the samples calcined at various temperatures, it was found that the intensity of the broadband covering the wide range between 3000 and 3700 cm^{-1} and vibrating band centered ~ 1627 cm^{-1} decreased with increasing calcination temperature. This is attributed to a reduction in the water molecules along with some organic impurities of the samples with increased calcination temperature. Considering the effect of temperature on the structural transformation of Co_3O_4, a slight shift of the peaks at about 572 and 667 cm^{-1} to a higher wavenumber is observed. It was also observed that the peak at about 592 cm^{-1} was particularly pronounced in the C8 sample, which could be due to the change in surface defects when the calcination temperature is increased.

The morphology of Co_3O_4 particles calcined at different temperatures of 400, 600, and 800 °C was investigated using the FESEM technique. The result is shown in Fig. 2. It can be clearly seen that the as-synthesized Co_3O_4 particles have an approximately polygonal shape with a strong agglomeration of fine-grained particles. In Fig. 2(a), it can be seen that in the sample calcined at 400 °C, the particles were relatively agglomerated and exhibited magnetic behavior, which was more pronounced in the very small Co_3O_4 particles than in the C6 and C8 samples. Therefore, it is quite difficult to determine the exact mean value of the particle size of the sample because the magnetic field leads to blurred microimages. Higher calcination temperatures resulted in significant grain growth of the particles. As shown in Figs. 2(a), 2(b), and 2(c), the average particle size was estimated from the micrographs and was 38.3 ± 5.7 nm, 94.6 ± 15.6 nm, and 379.9 ± 81.2 nm for calcination at 400, 600, and 800 °C, respectively. The large standard deviation is related to the distribution of size over a large area and the asymmetric shape of the particles. Figure 3 shows the microstructure of Co_3O_4 calcined at different temperatures investigated by TEM. In the figure, the continuous arrangement of particles without boundaries between the Co_3O_4 grains can be observed, especially for the C4 and C6 samples. This could be due to the magnetic properties that occur in the nanometer-sized

Table 1 The average crystallite size, lattice parameter, and average particle size evaluated by FESEM and TEM, specific surface area, pore volume, and average pore size of Co_3O_4 NPs calcined at different temperatures

Samples	Crystallite size (nm)	Lattice parameter, *a* (Å)	FESEM particle size (nm)	TEM particle size (nm)	Surface area (m^2/g)	Pore volume (cm^3/g)	Average pore size (nm)
C4	19.3 ± 1.4	8.089	38.3 ± 5.7	34.1 ± 4.0	133.2	0.57	16.2
C6	43.2 ± 4.2	8.084	94.6 ± 15.6	99.9 ± 22.6	103.1	0.44	29.2
C8	98.0 ± 5.2	8.083	379.9 ± 81.2	294.3 ± 49.3	67.5	0.13	56.5

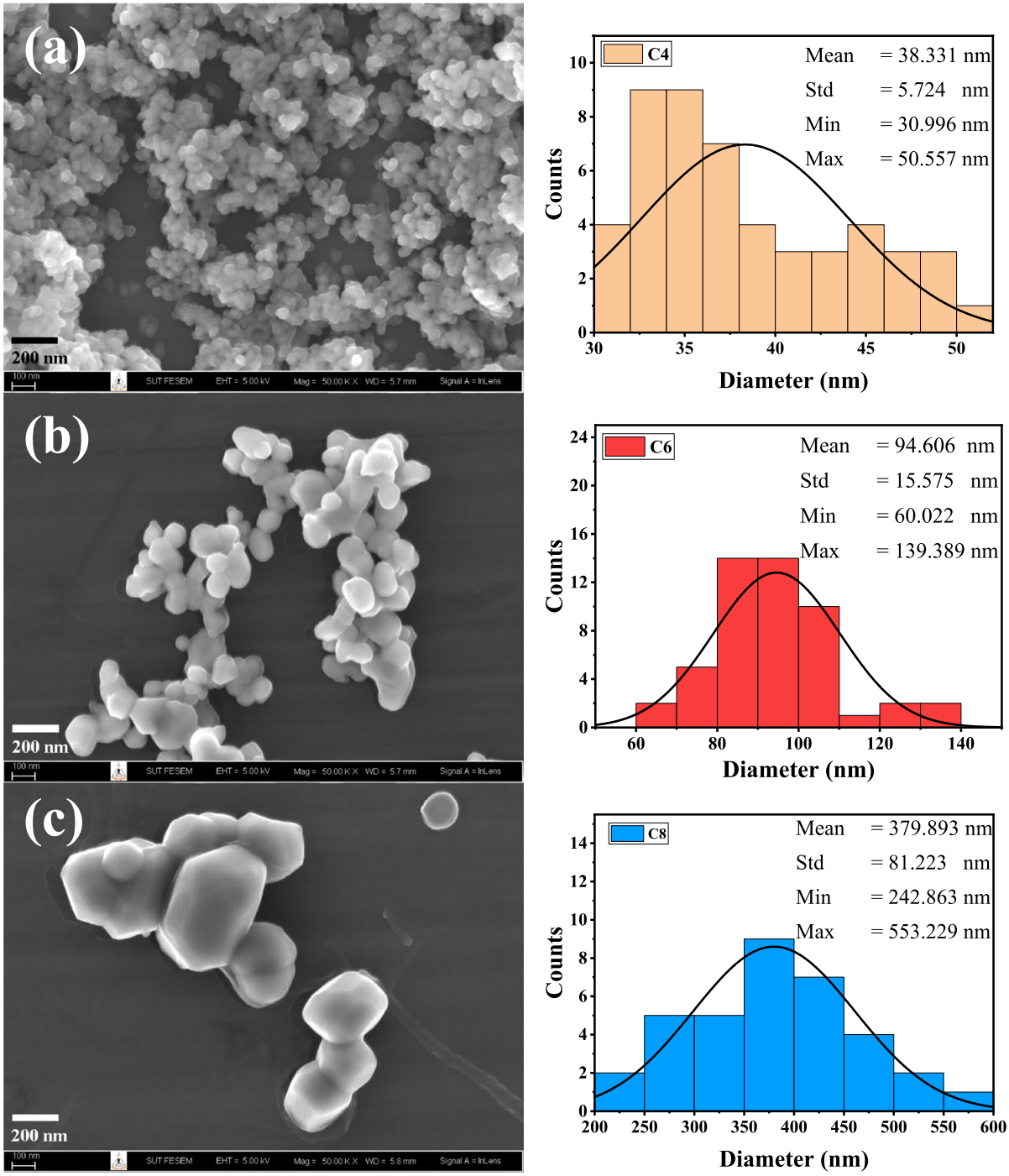

Fig. 2 Morphologies and particle size distribution curves of Co_3O_4 calcined at **a** 400, **b** 500, and **c** 600 °C studied by FETEM

Co_3O_4 particles. The average particle sizes of the samples were determined by measuring the equivalent diameters of the particles from each TEM image, see Figs. 3(a-1), 3(b-1), and 3(c-1). These results are listed in Table 1. It can be seen that the average particle sizes of the C4, C6, and C8 samples are

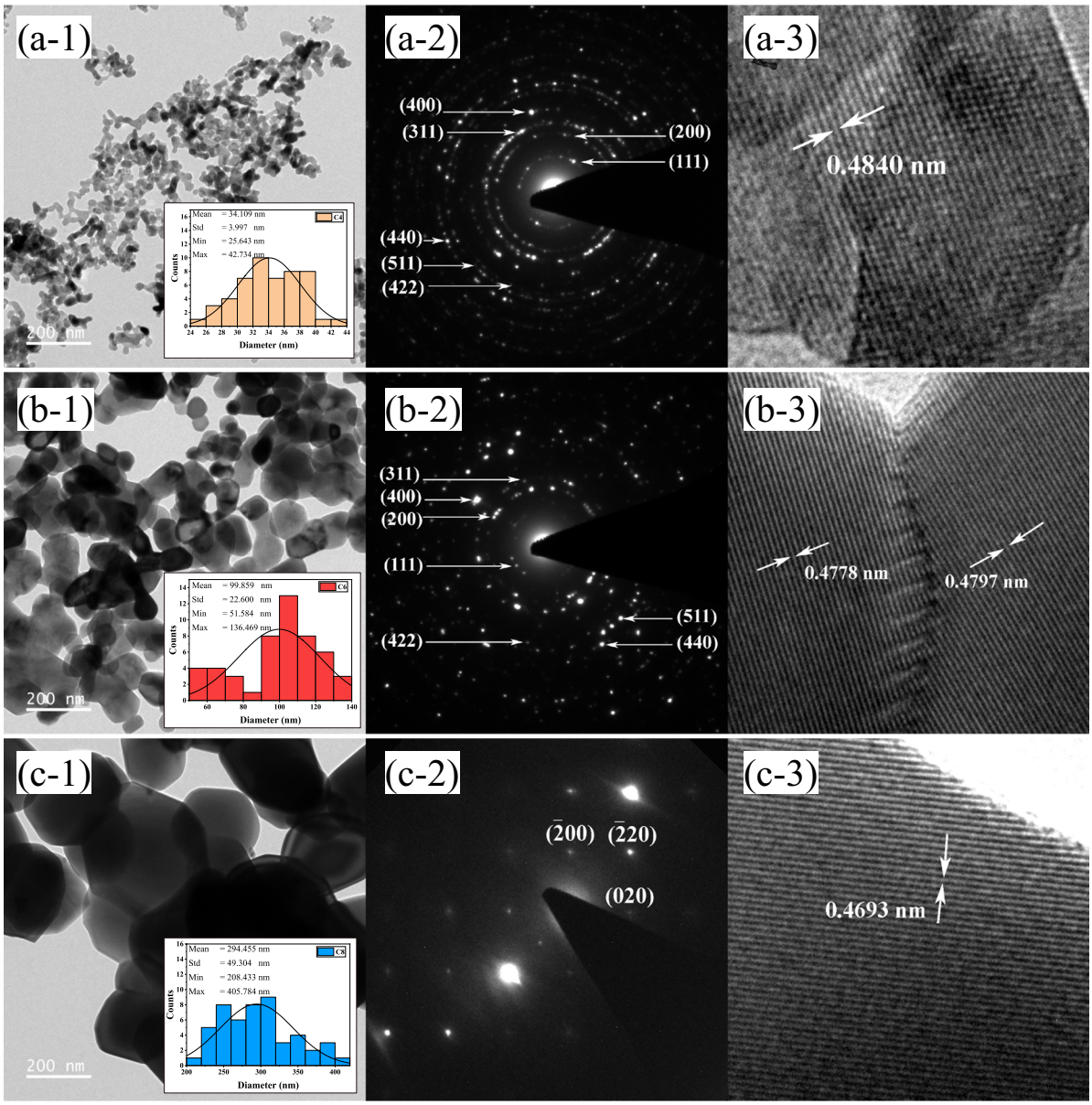

Fig. 3 Microstructure of **a** C4, **b** C6, and **c** C8 investigated by **1** TEM, **2** HRTEM, and **3** SAED techniques

34.1 ± 4.0 nm, 99.9 ± 22.6 nm, and 294.3 ± 49.3 nm, respectively. The lower deviation indicates a good uniformity of the particle size of the prepared C4 sample compared to the other samples. The increasing particle size with increasing temperature is probably due to the effect of thermal energy on ion diffusion at grain boundaries, which causes the growth of Co_3O_4 particles with increasing agglomeration [15]. Compared to the C4 sample, abnormal grain growth was found more frequently in calcined samples with higher temperatures. As a result, the average particle size of C8 is larger and exhibits higher variability compared to other samples. The corresponding selected electron diffraction patterns of C4, C6, and C8 are shown in Figs. 3(a-2), 3(b-2) and 3(c-2), respectively. The spotty ring SAED patterns shown in Figs. 3(a-2) and 3(b-2) are related to the polycrystalline cubic structure of Co_3O_4, while the

neatly arranged point diffraction patterns shown in Fig. 3(c-2) are from a single crystal with large grains in the submicrometer range of the cobalt tetraoxide particles. From the microstructural results, the lattice spacing of about 0.4667 nm is related to the (111) plane of the cubic spinel structure of Co_3O_4. It can be seen that the decrease of interplanar spacing from 0.4840 to 0.4693 nm, as shown in Figs. 3(a-3), 3(b-3), and 3(c-3), with the temperature of heat treatment, is consistent with the change of lattice constant and crystallite size obtained by X-ray diffraction analysis.

The chemical composition and valence states of all elements on the surfaces of the Co_3O_4 particles were investigated by XPS. These results are reported in Fig. 4. Figure 4(a) shows that the XPS survey spectra represent the major elemental components in the calcined samples, including Co2p, O1s, and C1s, which correspond to binding energies of 779.8, 529.8, and 284.8 eV, respectively. The spectra indicate the presence of cobalt, oxygen, and carbon on the surfaces of the samples. Overall, the XPS patterns of the samples calcined at different temperatures appeared to be similar, but different peak intensities were observed. The higher peak intensity with increasing calcination temperature was possibly due to the fact that the intensity of the XPS spectrum is directly proportional to the area under the peak. Therefore, the increase in peak intensity observed for the calcined sample at high temperature indicates a quantitative increase in the chemical states corresponding to the individual elements on the surface of the material. The XPS peaks corresponding to Co 2p and O 1 s were recorded in high-resolution mode, as shown in Figs. 4(b) and 4(c), respectively. Figure 4(b) shows that the two main peaks centered at binding energies of 779.8 and 794.7 eV can be ascribed to Co 2p3/2 and Co 2p1/2, respectively. In addition, there were two shake-up satellite peaks centered at 789.7 and 805.1 eV. The energy separation of the Co 2p spin orbit, 2p3/2, and 2p1/2 is approximately 15.34 eV, coupled with the occurrence of satellite peaks about 6 eV above the main peaks. This indicates the presence of Co^{3+} and Co^{2+} states in Co_3O_4 [18, 19]. From the O1s spectra corresponding to all samples as shown in Fig. 4(c), the deconvoluted peaks were fitted by the Gaussian function and the analysis results are summarized in Table S1. It can be seen that the O1s peaks were deconvoluted into three main peaks at 530.0 ± 0.2 eV, 531.3 ± 0.1 eV, and 532.3 ± 0.2 eV, which can be attributed to the lattice oxygen (O_{latt}) of the cubic spinel phases, the adsorbed O^{2-} ions (O_{ad}) in the oxygen-deficient region within Co_3O_4 (oxygen vacancies) and chemisorbed and associated oxygen species (O_2^-, O^{2-}, or O^-) and OH^- (O_{OH}) on the surface of the Co_3O_4 particles, respectively [19–21]. It is noticeable that peaks at 528.9 eV (4.2%), 529.3 eV (17.7%), 529.2 eV (5.3%), and 533.4 eV (2.7%) were found in the XPS spectra of the C4, C6, and C8 samples, respectively. These peaks probably originate from an artifact of fitting asymmetric XPS peaks with symmetric Gaussian functions [22]. It is noteworthy that the integrated intensity and energy position corresponding to O_{latt}^- peaks increased when the calcination temperature reached 800 °C. This indicates a complete spinel phase formation and a more ordered arrangement of the lattices on the sample surfaces. In addition, it was also observed that higher temperatures lead to a decrease in the defect state associated with oxygen vacancies, so the maximum oxygen vacancies in the C4 sample could be a significant factor affecting the electrochemical efficiency of this material [23]. The C element associated with the XPS peaks can be attributed to extrinsic hydrocarbon from the XPS device itself. It can be seen that the XPS results agree well with those of XRD and FTIR.

Figures 5(a) and 5(b) show the N_2 isotherms and the corresponding pore size distribution curves of the C4, C6, and C8 samples, respectively. Based on the International Union of Pure and Applied Chemistry (IUPAC) classification, the isotherms of all samples can be categorized as type IV with H3 hysteresis loops [19, 24]. This is consistent with a characteristic mesoporous structure with pore diameters between 2 and 50 nm and a slit-like shape formed by agglomerated Co_3O_4 nanoparticles [25]. As shown in Fig. 5(b), the porosity of the samples consisted of mesopores with pore sizes of 2–50 nm and macropores with pore diameters larger than 50 nm. The parameters related to the surface properties, including the BET specific surface area, the total pore volume, and the average BJH pore diameters of all samples are summarized in Table 1. The result shows that the C4 sample had the highest specific surface area of 133.2 m^2/g. The other samples showed a

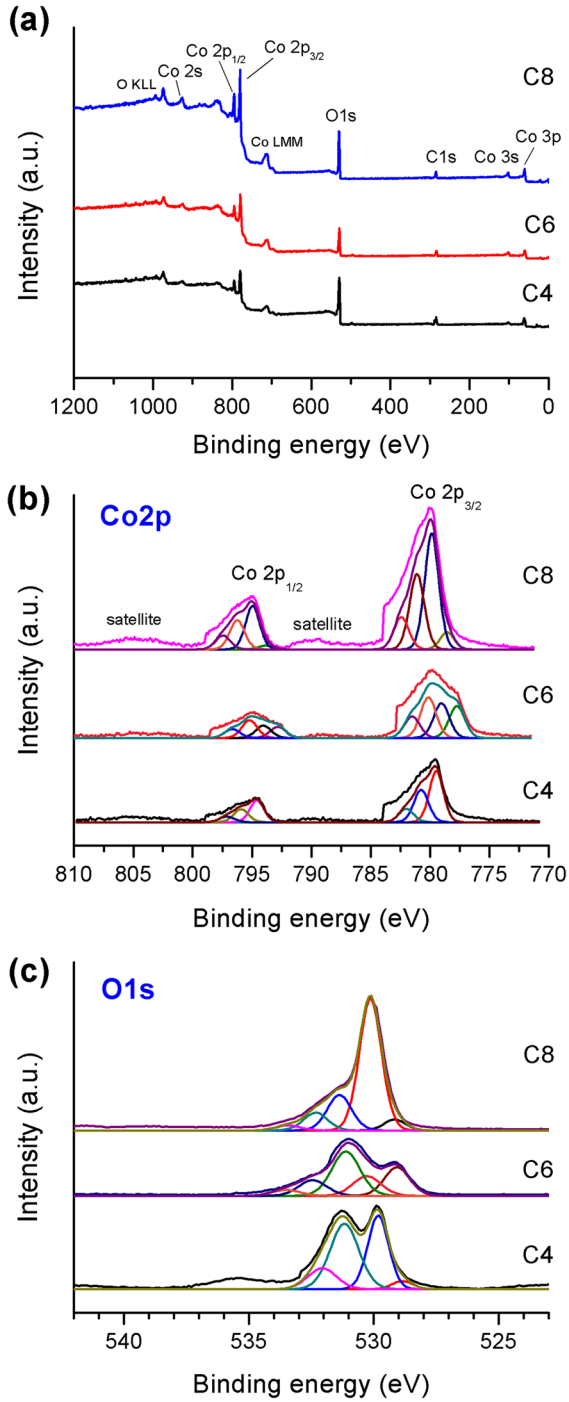

Fig. 4 X-ray photoelectron spectra of the C4, C6, and C8 samples **a** survey wide range, **b** Co2p, and **c** O1s spectra

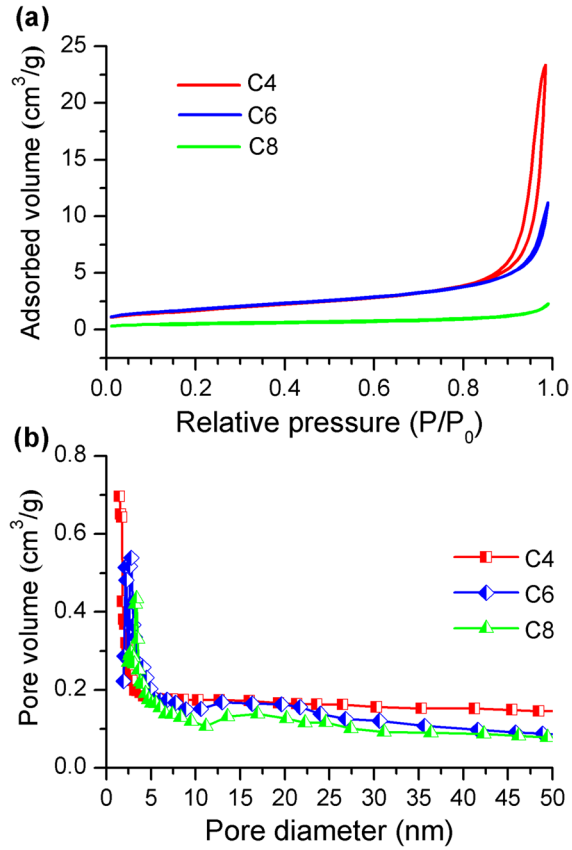

Fig. 5 **a** N_2 adsorption–desorption isotherms and **b** the corresponding pore size distributions of the C4, C6, and C8 samples

lower surface area of 103.1 and 67.5 m^2/g at calcination temperatures of 600 and 800 °C, respectively. Compared to the calcination temperatures, the total pore volume of the samples decreases from 0.57 to 0.13 cm^3/g when the temperature is increased from 400 to 800 °C. Moreover, the BJH average pore sizes increased from 16.2 to 56.5 nm when the temperatures were increased from 400 to 800 °C. This suggests that increased thermal energy not only leads to the growth of Co_3O_4 grains, increasing the particle size but also decreases the porosity of the materials. It can be said that the high pore volume and small pore size are directly related to the high porosity and specific surface area of the C4 sample. With respect to electrode applications, a large surface area and a suitable pore size are the most important factors affecting charge transport between the oxide surface and the electrolyte. This is directly related to the specific capacitance of a capacitor [26, 27]. The electrochemical properties of the electrode films prepared from the fabricated Co_3O_4 particles

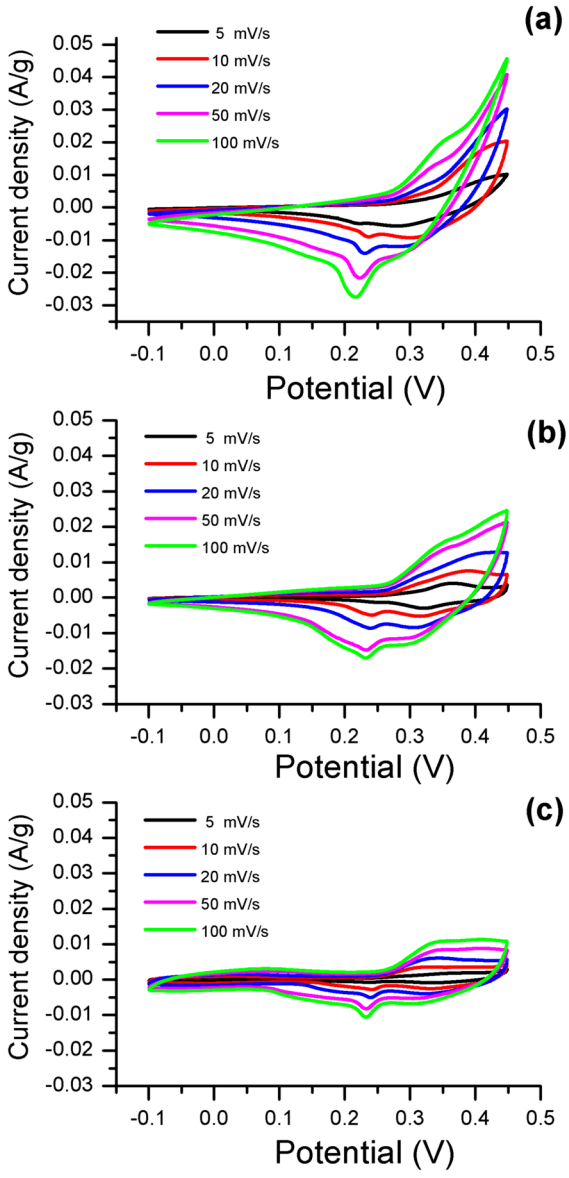

Fig. 6 CV curves of **a** C4, **b** C6, and **c** C8 electrodes performed at the different scan rates

were measured and are described in the following section.

Electrochemical examinations

To investigate the electrochemical properties of the prepared electroactive materials, CV, GCD, and EIS were employed. In this work, the CV technique was carried out at scan rates of 5, 10, 20, 50, and 100 mV/s over an applied potential range of − 0.10 to 0.45 V using an aqueous solution of 6 M KOH as electrolyte. As can be seen in Fig. 6, the cyclic voltammograms of all samples are analogous to the electrical double layer and pseudocapacitive properties. The distinction between anodic and cathodic peaks is correlated with oxidation and reduction reactions, respectively. These are determined by surface Faradaic processes occurring at or near the surfaces of Co_3O_4 electrodes [28]. Considering the reversible redox state of Co ions, it is possible that the anodic and cathodic peaks occurring in the potential ranges of 0.3–0.4 V and 0.2–0.3 V, respectively, are due to reversible redox reactions between Co^{3+}/Co^{4+} and Co^{3+}/Co^{2+}, respectively [27, 29]. The analytical results strongly indicate the favorable pseudocapacitive properties of Co_3O_4 electrodes. The Faradaic redox processes occurring in an alkali medium can be described by the following equations [30, 31]:

$$Co_3O_4 + OH^- + H_2O \rightleftarrows 3CoOOH + e^- \quad (2)$$

$$CoOOH + OH^- \rightleftarrows CoO_2 + H_2O + e^- \quad (3)$$

From the appropriate voltammograms, the specific capacitance (C_s) of Co_3O_4 electrodes at different scan rates can be calculated using the following equation [12]:

$$C_s = \int \frac{IdV/V}{m\Delta V} \quad (4)$$

where $\int IdV$ is an integral area under the CV curves, m is mass of the active material, V is the scan rate, and ΔV is the applied potential window. The calculated C_s values for the different electrodes are given in Table 2.

It can be clearly seen in Table 2 that the C4 electrode has a higher specific capacitance at all scan rates examined. This corresponds to a larger area under the CV curve than for the C6 and C8 electrodes. The intensity of redox peaks and the shift of anodic and cathodic peak positions to higher values were found when the scan rate was increased from 5 to 100 mV/s, as shown in Fig. 6. This result contributes to the change in specific capacitance of the samples as C_s tend to decrease with increasing scan rate. At higher scan rates, the OH- diffusion is reduced and the ions can only reach the outer surface of the electrodes. Since the ion accumulation on the surface of the electrodes is limited,

the capacitance values decrease [32]. It has been reported that when the electrode material has high porosity, i.e., high pore volume and large specific surface area, the reduction of electrons and ion diffusion pathways are impacted, resulting in more active sites. This promotes electrochemical reactions and consequently increases the capacitive performance of the devices [32–34]. In the present work, the highest specific capacitance, 117.3 F/g, was obtained with a C4 electrode at a scan rate of 5 mV/s. This is due to the fact that the C4 sample had the highest specific surface area and porosity among the samples.

Figures 7(a)–(c) show GCD curves of C4, C6, and C8 at different current densities of 1, 2, 5, 10, and 20 A/g, respectively. From these figures, it can be seen that there are two different charging and discharging processes. Considering the first part of the GDC curve, the discharge process below 0.2 V, the curve parallel to the potential axis shows a pure double-layer capacitance behavior due to the charge separation at the electrode/electrolyte interface. In the second part (0.2–0.45 V), the sloped curve corresponds to a capacitive component due to pseudocapacitance arising from electrochemical adsorption–desorption or redox reactions at the electrode/electrolyte interface [32, 35, 36]. In addition, the initial state of the discharge process may reflect a resistive component arising from a sudden voltage drop representing the voltage change due to an equivalent series resistance (ESR) [28, 37]. Compared to the C4 electrode, the rapid increase in the slope of the discharge curve with current density, as seen in Figs. 7(a)–(c), indicates a higher internal resistance and results in less ion diffusion at the surfaces of the C6 and C8 electrodes. As a result, the discharge time becomes shorter, and the specific capacitance possibly decreases. From the results of GCD, the specific capacitance (C_{GCD}) can be calculated using the following equation [36, 38]:

$$C_{GCD} = \frac{I\Delta t}{m\Delta V} \tag{5}$$

where I is an applied current density, Δt is the discharge time, m is mass of the active material, and ΔV is applied potential window during the discharge process. Calculated discharge-specific capacitance values of the C4, C6, and C8 electrodes are summarized in Table 2. The variation of specific capacitance as a function of current density of different electrodes is presented in Fig. 7(d). It can be seen that the C_{GCD} values decreased with increasing current density. Furthermore, variation in specific capacitance of the different electrodes was in accordance with the C_s values obtained from the CV technique, i.e., the highest specific capacitance is found in the C4 electrode. The maximum C_{GCD}, 115.3 F/g, can be achieved at a current density of 1 A/g. This may be attributed to higher porosity and specific surface area coupled with better permeability of charges and ions at the electrode/electrolyte interface of the C4 sample than for other samples.

The cycling performance of an electrode is an important parameter in practical applications. Therefore, the long-term cycling performance of the C4 electrode was further investigated at a current density of 5 A/g for 5000 cycles. The results are shown in Fig. 8. Typically, the electrolyte on the electrode surface decomposes with increasing cycling time, resulting in increased irreversible charging capacity and consequently lower specific capacitance [38]. The excellent cycling stability with a retention efficiency of 100% was maintained for 1900 cycles. Thereafter, the specific capacitance gradually decreased from 82.4 to 81.0 F/g after 5000 cycles, corresponding to a capacitive retention of 98%. This indicates excellent electrochemical stability of the as-prepared C4 electrode. Interestingly, the cycling stability of the fabricated electrode is higher than the performance reported in

Table 2 The specific capacitances of the electroactive materials calculated using cyclic voltammograms (C_s) and chronopotentiograms (C_{GCD})

Samples	C_s (F/g)					C_{GCD} (F/g)				
	Scan rate (mV/s)					Current density (A/g)				
	5	10	20	50	100	1	2	5	10	20
C4	117.3	95.6	72.6	56.1	38.3	115.3	98.4	81.5	66.6	45.3
C6	95.7	81.4	67.7	50.3	31.2	94.6	86.9	72.8	54.1	33.4
C8	61.4	45.8	36.2	23.9	14.6	58.7	46.4	39.8	23.1	15.2

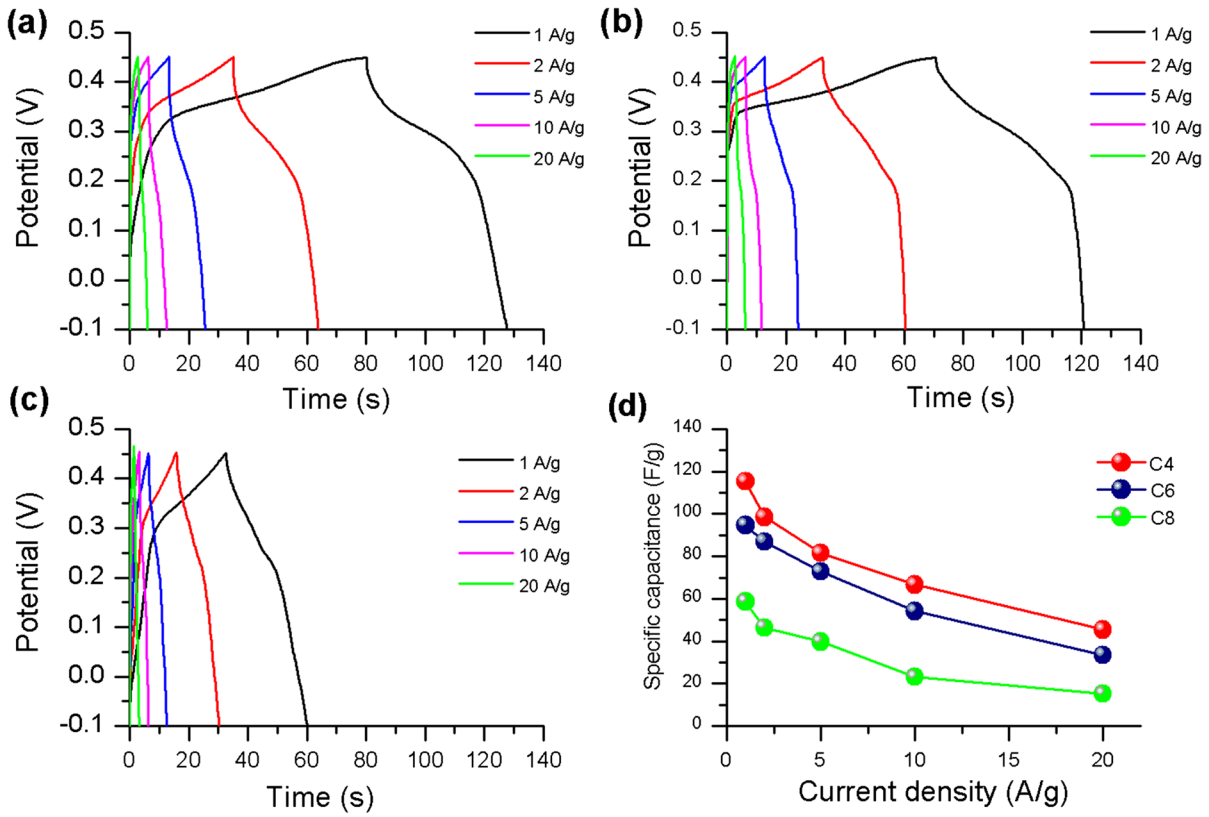

Fig. 7 GCD curves of **a** C4, **b** C6, and **c** C8 electrodes at different current densities and **d** the change in specific capacitance as a function of current density

previous works [12, 32, 33, 36]. The inset in Fig. 8 shows the charge–discharge behavior of the C4 sample at a current density of 1 A/g within a voltage window from − 0.1 to 0.45 V. Additionally, the Coulombic efficiency (η), a parameter indicating the feasibility of a redox process, can be calculated using the following equation [39, 40]:

$$\eta = \frac{t_D}{t_C} \times 100\% \tag{6}$$

where t_D and t_C are discharging and charging total, respectively. In the first three cycles of the charge/discharge process, the Coulombic efficiency is below 100%, indicating an irreversible capacity loss in the prepared cells. This can be attributed either to the blocking penetration of the liquid electrolyte into the porous structured Co_3O_4 materials at the initial state of the measurement or to the irreversible formation of the solid electrolyte interface and the decomposition of the electrolyte [41, 42]. Then, a Coulombic efficiency of ~100% can be interpreted as a possible redox process of electrode material during the charge–discharge processes. Extended cycling tests can be performed without significantly damaging the microstructure of the material [28]. As can be seen in Fig. 8, there was no significant change in charge–discharge over 5000 cycles. This shows that the as-prepared Co_3O_4 nanoparticles calcined at 400 °C have high pseudocapacitance and good cyclability, indicating that they are a promising electrode material for supercapacitor applications.

Electrochemical impedance spectroscopy was performed to understand the fundamental charge transport behavior of Co_3O_4 electrodes. The corresponding Nyquist plots of the different electrodes in Fig. 9(a) were modeled with an equivalent circuit shown in Fig. 9(b). R_s is the internal solution resistance, which includes the intrinsic resistance of the electrolyte, contact, and electrode material. R_{ct} is the charge transfer resistance caused by the Faradaic reactions

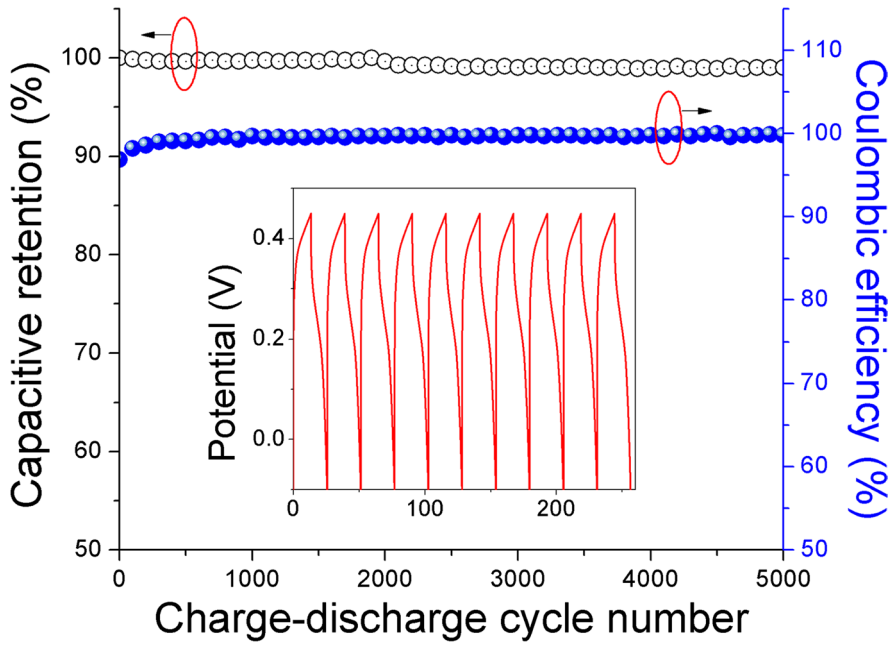

Fig. 8 The capacitance retention and Coulombic efficiency of the C4 electrode for 5000 cycles at a current density of 5 A/g

occurring at the electrode surface. CPE is the constant phase element to account for the double-layer capacitance. Z_w is the Warburg impedance related to the diffusion of ions [43]. In Fig. 9(a), it can be seen that the Nyquist diagrams for the different electrodes are similar. They show a semicircular region in the high-frequency region and a straight line in the low-frequency region, as shown in the inset of Fig. 9(a). The Warburg section is shown between the semicircular arc and the line. The high-frequency intercepts on the real axis correspond to R_s values of 0.31, 0.31, and 0.32 for the C4, C6, and C8 electrodes,

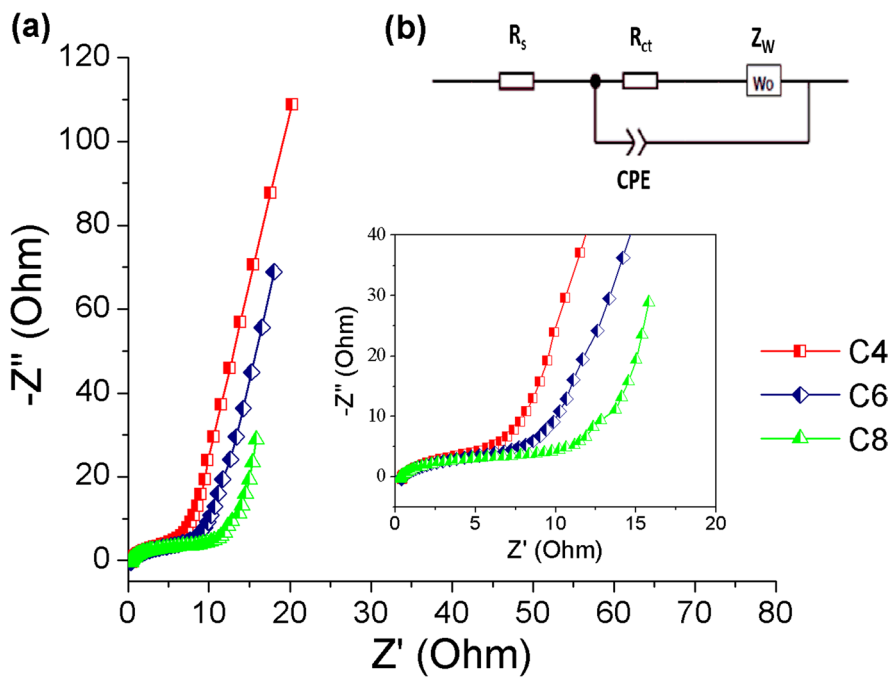

Fig. 9 **a** Nyquist plots of the different electrodes with the magnified impedance spectra in the high-frequency region (inset) and **b** the corresponding equivalent circuit

respectively. The semicircular arcs correspond to R_{ct} values of 6.18, 8.18, and 12.06 for the C4, C6, and C8 electrodes, respectively. The lowest R_s and R_{ct} values clearly indicate that the C4 electrode has higher electrical conductivity than the C6 and C8 samples. This facilitates charge transport at the interface between the electrode and the electrolyte. The present results suggest that the crystal structure, microstructure including particle size, pore size, pore volume and specific surface area, and electrical conductivity are all key factors promoting the excellent electrochemical performance of the C4 sample.

Conclusions

The present work demonstrates a facile and inexpensive synthesis of Co_3O_4 nanoparticles for use as working electrodes of supercapacitors. The crystal structure showed that the Co_3O_4 calcined at different temperatures exhibited a normal cubic spinel structure. The crystallite size increased with calcination temperature. The morphological properties were studied and it was found that all the samples exhibited polygonal shapes with average particle sizes ranging from 34.1 ± 4.0 nm to 294.3 ± 49.3 nm. The N_2 adsorption–desorption results showed that the sample calcined at 400 °C had the highest specific surface area and pore volume (133.2 m^2/g and 0.57 cm^2/g, respectively). Electrochemical characterization of the as-prepared Co_3O_4 showed that all samples exhibited intrinsic pseudocapacitive properties. The highest specific capacitance, 115.3 F/g, was obtained at a current density of 1 A/g. Higher cyclic stability was achieved with the C4 electrode at a current density of 5 A/g. This can be attributed to the superior electrical conductivity and high purity of the phase structure with a larger specific surface area and high porosity of the C4 material. Moreover, the different oxidation states of Co ions in electrochemical reactions are the main factor for the high capacitance values. The results of the current study indicate the possibility of further developing the mass production of Co_3O_4 for supercapacitor applications.

Acknowledgements The authors would like to thank the Department of Physics, Faculty of Science, Khon Kaen University, for use of their electrochemical workstation facility. This research project was financially supported by Mahasarakham University.

Data availability The authors declare that all relevant data are included in the article and/or its supplementary information files.

Compliance with ethical standards

Conflict of interest The authors declare that they have no conflicts of interest.

References

1. Jule LT, Dejene FB, Ali AG, Roro KT, Hegazy A, Allam NK, El Shenawy E (2016) Wide visible emission and narrowing band gap in Cd-doped ZnO nanopowders synthesized via sol-gel route. J Alloys Compounds 687:920–926
2. Ahmed F, Arshi N, Dwivedi S, Koo BH, Azam A, Alsharaeh E (2016) Low temperature growth of ZnO nanotubes for fluorescence quenching detection of DNA. J Mater Sci Mater Med 27:189–189
3. Lee WC, Fang Y, Turner JFC, Bedi JS, Perry CC, He H, Qian R, Chen Q (2016) An enhanced gas ionization sensor from Y-doped vertically aligned conductive ZnO nanorods. Sens Actuator B: Chem 237:724–732
4. Yang T, Chen M, Kong Q, Luo X, Jiao K (2017) Toward DNA electrochemical sensing by free-standing ZnO nanosheets grown on 2D thin-layered MoS_2. Biosens Bioelectron 89:538–544
5. Makhlouf SA, Bakr ZH, Aly KI, Moustafa MS (2013) Structural, electrical and optical properties of Co_3O_4 nanoparticles. Superlattice Microst 64:107–117
6. Twilton J, Le C, Zhang P, Shaw MH, Evans RW, MacMillan DWC (2017) The merger of transition metal and photocatalysis. Nat Rev Chem 1:0052
7. Bai S, Liu H, Sun J, Tian Y, Luo R, Li D, Chen A (2015) Mechanism of enhancing the formaldehyde sensing properties of Co_3O_4 via Ag modification. RSC Adv 5:48619–48625
8. Salavati-Niasari M, Khansari A, Davar F (2009) Synthesis and characterization of cobalt oxide nanoparticles by thermal treatment process. Inorg Chim Acta 362:4937–4942
9. Lu Y, Deng B, Liu Y, Wang J, Tu Z, Lu J, Xiao X, Xu G (2021) Nanostructured Co_3O_4 for achieving high-performance supercapacitor. Mater Lett 285:129101
10. Wadekar KF, Nemade KR, Waghuley SA (2017) Chemical synthesis of cobalt oxide (Co_3O_4) nanoparticles using Co-precipitation method. Res J Chem Sci 7:53–55
11. Meher SK, Rao GR (2011) Ultra layered Co_3O_4 for high-performance supercapacitor applications. J Phys Chem C 115:5646–15654
12 Li Y, Wu H, Wu Y, Li Q (2017) Facile synthesis of mesoporous Co_3O_4 nanowires for application in supercapacitors. J Mater Sci Mater Electron 28:16826–16835
13. Lin KS, Chowdhury S (2010) Synthesis, characterization and application of 1-D cerium oxide nanomaterials. Int J Mol Sci 11:3226–3251
14. Kurajica S, Minga I, Gulis M, Mandit V, Van Simcic I (2016) High surface area ceria nanoparticles via hydrothermal synthesis experiment design. J Nanomater 10:1–8

15. AnandhaBabu G, Ravi G, Hayakawa Y, Kumaresavanji M (2015) Synthesis and calcinations effects on size analysis of Co_3O_4 nanospheres and their superparamagnetic behaviors. J Magn Magn Mater 375:184–193
16. Naveen AN, Selladurai S (2014) Investigation on physiochemical properties of Mn substituted spinel cobalt oxide for supercapacitor applications. Electrochim Acta 125:404–414
17. Stella C, Soundararajan N, Ramachandran K (2015) Structural, optical, and magnetic properties of Mn and Fe-doped Co_3O_4 nanoparticles. AIP Adv 5:087104
18. Patil D, Patil P, Subramanian V, Joy PA, Potdar HS (2010) Highly sensitive and fast responding CO sensor based on Co_3O_4 nanorods. Talanta 81:37–43
19. Huang H, Zhu W, Tao X, Xia Y, Yu Z, Fang J, Gan Y, Zhang W (2012) Nanocrystal-constructed mesoporous single-crystalline Co_3O_4 nanobelts with superior rate capability for advanced lithium-ion batteries. ACS Appl Mater Interfaces 4:5974–5980
20. Roginskaya YE, Morozova O, Lubnin E, Ulitina YE, Lopukhova G, Trasatti S (1997) Characterization of bulk and surface composition of $Co_xNi_{1-x}O_y$ mixed oxides for electrocatalysis. Langmuir 13:4621–4627
21. Lü Y, Zhan W, He Y, Wang Y, Kong X, Kuang Q, Xie Z, Zheng L (2014) MOF-templated synthesis of porous Co_3O_4 concave nanocubes with high specific surface area and their gas sensing properties. ACS Appl Mater Interfaces 6:4186–4195
22. Shou Z, Zhang Y, Wang Z, Wei W, Teng W, Shi J, Xiong R (2008) Electronic structure studies of the spinel $CoFe_2O_4$ by X-ray photoelectron spectroscopy. Appl Sur Sci 254:6972–6975
23. Li N, Du K, Liu G, Xie Y, Zhou G, Zhu J, Li F, Cheng HM (2013) Effects of oxygen vacancies on the electrochemical performance of tin oxide. J Mater Chem A 1:1536–1539
24. Park JS, Shin DO, Lee CS, Young-Gi L, Kim JY, Kim KM, Shin K (2018) Mesoporous perforated Co_3O_4 nanoparticles with a thin carbon layer for high performance Li-ion battery anodes. Electrochim Acta 264:376–385
25. Kanjana N, Maiaugree W, Poolcharuansin P, Laokul P (2020) Size controllable synthesis and photocatalytic performance of mesoporous TiO_2 hollow spheres. J Mater Technol 48:105–113
26. Simon P, Gogotsi Y (2008) Materials for electrochemical capacitors. Nat Mater 7:845–854
27. Wang Y, Lei Y, Li J, Gu L, Yuan H, Xiao D (2014) Synthesis of 3D-nanonet hollow structured Co_3O_4 for high capacity supercapacitor. ACS Appl Mater Interfaces 6:6739–6747
28. Lima-Tenório MK, Ferreira CS, Rebelo QHF, Brambilla de Souza RF, Passos RR, Gómes Pineda EA, Pocrifka LA (2018) Pseudo capacitance properties of Co_3O_4 nanoparticles synthesized using a modified sol-gel method. Mater Res 21(2):1–7
29. Cao L, Xu F, Liang YY, Li HL (2004) Preparation of the novel nanocomposite $Co(OH)_2$/ultra-stable Y zeolite and its application as a supercapacitor with high energy density. Adv Mater 16:1853–1857
30. Casella IG, Gatta M (2002) Study of the electrochemical deposition and properties of cobalt oxide species in citrate alkaline solutions. J Electroanal Chem 534:31–38
31. Svegl F, Orel B, Hutchins M, Kalcher K (1996) Structural and spectroelectrochemical investigations of sol-gel derived electrochromic spinel Co_3O_4 films. J Electrochem Soc 143:1532–1539
32. Zhang F, Hao L, Zhang L, Zhang X (2011) Solid-State thermolysis preparation of Co_3O_4 nano/micro superstructures from metal-organic framework for supercapacitors. Int J Electrochem Sci 6:2943–2954
33. Tummala R, Guduru RK, Mohanty PS (2012) Nanostructured Co_3O_4 electrodes for supercapacitor applications from plasma spray technique. J Power Sources 209:44–51
34. Wang DW, Li F, Liu M, Lu GQ, Cheng HM (2008) 3D aperiodic hierarchical porous graphitic carbon material for high rate electrochemical capacitive energy storage. Angew Chem Int Edition 120:379–382
35. Shan Y, Gao L (2007) Formation and characterization of multi-walled carbon nanotubes/Co_3O_4 nanocomposites for supercapacitors. Mater Chem Phys 103(2–3):206–210
36. Xiong S, Yuan C, Zhang X, Xi B, Qian Y (2009) Controllable synthesis of mesoporous Co_3O_4 nanostructures with tunable morphology for application in supercapacitors. Chem Eur J 15:5320–5326
37. Jagadale AD, Dubal DP, Lokhande CD (2012) Electrochemical behavior of potentiodynamically deposited cobalt oxyhydroxide (CoOOH) thin films for supercapacitor application. Mate Res Bull 47:672–676
38. Duan Y, Hu T, Yang L, Gao J, Guo S, Hou M, Ye X (2019) Facile fabrication of electroactive microporous Co_3O_4 through microwave plasma etching for supercapacitors. J Alloys Compounds 771:156–161
39. Zhang F, Yuan C, Zhu J, Wang J, Zhang X, Lou XW (2013) Flexible films derived from electrospun carbon nanofibers incorporated with Co_3O_4 hollow nanoparticles as self-supported electrodes for electrochemical capacitors. Adv Funct Mater 23:3909–3915
40. Wang D, Wang Q, Wang T (2011) Morphology-controllable synthesis of cobalt oxalates and their conversion to mesoporous Co_3O_4 nanostructures for application in supercapacitors. Inorg Chem 50:6482–6492
41. Danhua G, Hongbo G, Jiaqing W, Junwei Z, Yue P, Xueqin Cao C, Hongwei G (2014) Porous nano-structured Co_3O_4 anode materials generated from coordination-driven self-assembled aggregates for advanced lithium-ion batteries. Nanoscale 6:9689–9694
42. Bin W, Shifeng W, Yuanyuan T, Yaxiong J, Wei L, Xiao-Ying L (2019) Hydrothermal synthesis of mesoporous Co_3O_4 nanorods as high-capacity anode materials for lithium-ion batteries. Energy Procedia 158:5293–5298
43. Liu J, Jiang J, Bosman M, Fan HJ (2012) Three-dimensional tubular arrays of MnO_2-NiO nanoflakes with high areal pseudo capacitance. J Mater Chem 22:2419–2426